High-Gain High-Frequency Three-Phase LLC Resonant Converter Design Based on the Wye-Delta Transformer for Aircraft Applications

Daniel Ríos Linares, *Student Member, IEEE*, Alberto Delgado Expósito, *Member, IEEE*, and Miroslav Vasić, *Senior Member, IEEE*,

***Abstract*—The requirements for small form-factor power supplies drive the need for high-frequency, small magnetic components and high efficiency to obtain thermal stability. When combined with high output power, magnetic optimization becomes crucial in the pushing of the boundaries of magnetic shrinkage. Among those applications in need of power dense systems, aircraft is considered one of the most restrictive due to its ultra-high reliability and miniaturization in both volume and mass. Critical on-board apparatus upstream the responsibility to the power stage classifying it as mission-critical. The selection of a multiphase converter enables the desired magnetic components shrinkage. With these objectives in mind, a Three-Phase LLC based on the wye-delta transformer is selected as a promising topology to fulfil high efficiency, small form-factor, effective power density and high voltage step-down in aircraft applications. The focus of this work is the listing of the guidelines on the design of the three-phase magnetic components with the compensation of an asymmetric structure (EE/EI cores) to match its magnetic coupling. The multiple sources of power losses are analysed and optimized, including the high-amplitude high-frequency currents traveling around the PCB. This paper presents the design of an unidirectional DC/DC converter with an input voltage range of 235-285 V to 28 V at the output, controlled by a frequency range of 15 % for a nominal output power of 1 kW reaching 96 % of efficiency.**

***Index Terms*—LLC, three-phase, high frequency, high power density, high voltage step-down, DC/DC converter, coupled inductors, magnetic optimization**

NOMENCLATURE

LLC converter design

L_r	Resonant inductance
C_r	Resonant capacitance
L_μ	Magnetizing inductance
Z_r	Characteristic impedance of the resonant tank
Q	Quality factor of the resonant tank
ω_r	Resonant angular frequency
m	Total inductance to magnetizing ratio

Circuit voltages and currents

k	Identifier of the phase ($k = A, B, C, a, b, c$)
$i_{L_r,k}$	Current through the resonant tank for phase k
$v_{C_r,k}$	Voltage across the resonant capacitance for phase k
V_I	Input voltage (DC)
V_O	Output voltage (DC)
$\bar{U}_k$	Voltage across the windings (phasor)
$\bar{I}_k$	Current through the windings (phasor)

Magnetic design

$\hat{B}$	Peak of the B-field within the core
f_S	Switching frequency
T_S	Switching period
A_e	Effective cross-sectional area of the magnetics
n_p	Number of turns of the transformer (primary)
n_s	Number of turns of the transformer (secondary)
n	Winding turns ratio of the transformer

Eddy current power losses in a foil conductor

F_R	Correction factor for Eddy currents for foil conductor
t	Thickness of the foil (copper track)
δ	Skin effect depth
ν	Ratio between the skin depth and thickness
μ_{Cu}	Absolute permeability of the copper
ρ_{Cu}	Absolute resistivity of the copper
$\hat{I}$	Peak of the current through the conductor

I. INTRODUCTION

AIRCRAFT electronic applications introduce challenging conditions with an extensive regulatory basis. The half-brick format for power supplies constitutes a typical form factor in aircraft converters. This means that the converter is height-constrained, reducing the available space for the magnetic components. These volume and mass restrictions are correlated with the mandatory high efficiency, as the heat dissipation is challenging. Additionally, electromagnetic interference has to be under control as the power converters should not perturbate the on-board apparatus in mid-flight, establishing soft-switching topologies as a wise option and resonant converters as a promising choice.

LLC resonant converters possess all these features allowing the designer to increase the switching frequency due to its intrinsic Zero Voltage Switching (ZVS) on the entire load range allowing the shrinkage of the magnetic components and thus, increasing the power density. Contemporary GaN transistors with their low capacitance are the enablers of the high-frequency operation.

A very high voltage step-down DC/DC conversion is needed, as on-board equipment need 28 V DC to operate from a wide input voltage range (200 to 330 V) [1]. When developing high voltage gain in isolated converters, most of the conversion is achieved by the transformer windings ratio resulting into an overcrowded window for the magnetics as well as higher power losses due to proximity effects.

To solve it, single-staged converters are built upon multiple transformers to reduce current stresses [2], series-parallel

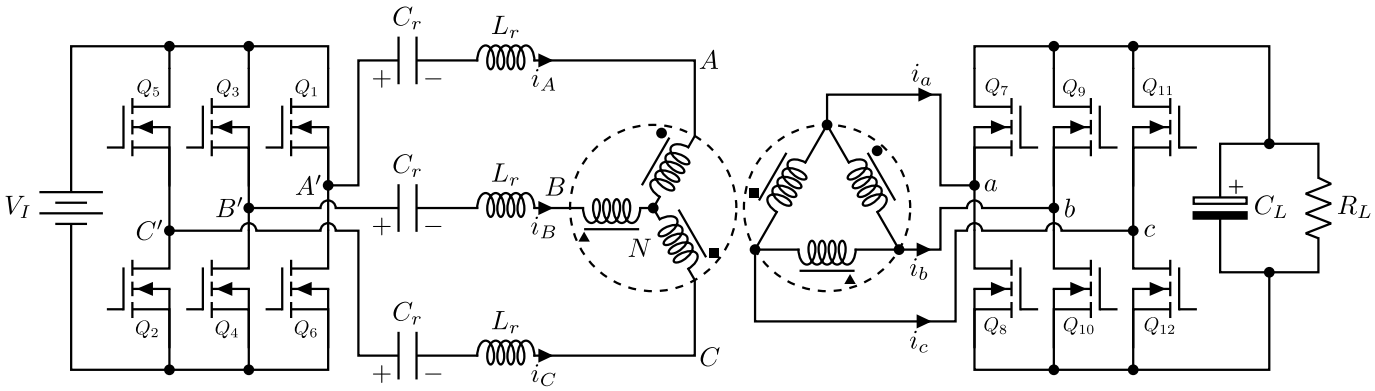

Fig. 1: Wye-Delta Three-Phase LLC Resonant Converter

multi-winding transformers can be employed [3], series converters are adopted [4] and matrix transformers are proposed [5]. Multi-staged solutions also can be found in the literature by interleaving LLC converters [6] or through series-parallel architecture [7]. Some scholars focus on the addition of other operating modes such as phase-shift modulation [8], multiple output [9] or pulse width and amplitude modulation [10].

Moreover, due to high input and output current ripple, the effective power density at system-level may be reduced as bigger filtering passive devices will have to be dimensioned.

These issues bring us to the implementation of a multiphase solution into the LLC converter family, as these topologies allow the designer to choose among different techniques to reduce the input and output current ripple [11], lessen the current per phase [12] or integrate magnetic components [13].

This multiphase concept can be applied at the inverter and rectifier, as in the three-phase LLC [14]. These ideas are still valid for center-tap rectification [15], full-bridge rectification [16], creating matrix transformers [11] or with interleaved structures within the three-phase configuration [12], [17].

Three-phase systems offer specific additional benefits, as three-phase inductors [18] and transformers [19] ensure the integration of magnetics down to two individual magnetic components. The arrangement of the windings of the transformer can be in wye-delta [19], delta-wye, delta-delta [15] and wye-wye [16]. The resonant capacitance arrangement into a delta configuration (Δ-C_r) [14] reduces the required individual value of capacitance. For all these reasons, the three-phase LLC converter is a promising candidate topology to be analyzed and optimized for high power density applications.

The need for a low-profile form factor converter mean that, due to the limited magnetic permeability of asymmetric magnetic cores, an electrical unbalance of these components becomes noticeable. This is not exclusive of the multiphase LLC converter but of any converter able to be configured in a multiphase manner such as the Dual Active Bridge (DAB) [20], and will be address in this research work with the compensation of the magnetic coupling between the columns of a EE/EI magnetic core.

TABLE I: Three-phase transformers turns ratio for unity gain

Feature	Wye-Wye	Wye-Delta	Delta-Delta	Delta-Wye
Voltage gain	1	$\sqrt{3}$	1	$1/\sqrt{3}$
Turns ratio	$1:1$	$1/\sqrt{3}:1$	$1:1$	$\sqrt{3}:1$

The low-profile of the converter makes it necessary to select a topology with inherent gain in order to minimize the number of turns required in the transformer and take full advantage of the topology. The three single-phase transformers can be connected into a single three-phase transformer, and among the different possible connections (wye, delta, zig-zag...), as shown in table I, the wye-delta transformer includes an intrinsic $\sqrt{3}$ step-down in the voltage conversion ratio (and a $\sqrt{3}$ step-up in the current) decreasing the voltage conversion ratio imposed on the winding turns ratio $n = n_p/n_s$ and helping further scaling of the LLC transformer.

This feature is crucial in this case as the specifications of the main line aircraft DC/DC converters have to step down the voltage from hundreds of volts to 28 V. In this paper, a 270-28 V, 1 kW, 900 kHz three-phase LLC based on the wye-delta transformer is analyzed in detail.

This paper presents a three-phase LLC DC/DC converter topology with a wye-delta transformer, a combination suitable to satisfy the high voltage gain required in aircraft applications. Insights on the operation of the topology will be exposed together with the design guidelines of the resonant tank to

TABLE II: Specifications for the converter

Parameter	Value	Description	
V_I	270 V	Nominal	Input voltage
	235-285 V	Normal	
	220-325 V	Abnormal	
V_O	28 V	Nominal	Output voltage
	26.6-29.4 V	Range	
P_O	1 kW	Nominal	Output power
	0-1 kW	Range	
ΔF_x	15 %	Normal	Frequency range
	100-1000 W	In range	
V_{ins}	2250 V	Minimum	Insulation
w	61 mm	Width	Converter dimensions
l	58 mm	Length	
h	13 mm	Height	

fulfil the strict operating frequency variation (10 % around the nominal switching frequency) as well as the range of the input voltage and output power to regulate the output to 28 V (the full specifications are shown in table II). The magnetic components geometry dimensioning will be proposed, eliminating the inherent asymmetry of three-port magnetic cores.

The contributions of the research outlined in the present work are as follows:

1) High gain, low-profile form factor: designing the converter in a low-profile form factor and for a wide input voltage range with frequency variation constraints is a key contribution for applications with restricted converter volume, such as avionics. The full design procedure is discussed: component selection, winding structure, practical application on the magnetics (transformer and inductor), analysis of the power losses and layout implications of the rectifier.
2) High efficiency: the emphasis on high efficiency is a significant contribution, especially in the context of aircraft applications where energy efficiency is critical for the overall system performance. Optimization of the converter in magnetics with flexibility in their design is considered, enabling their integration.
3) Balanced magnetic structure: the development of a balanced magnetic structure is crucial for the proper operation of the converter. This is achieved by producing an even magnetic flux distribution between columns (central and lateral columns while also maintaining among lateral columns). This balance is essential for optimal transformer performance in a Three-Phase LLC resonant converter contributing to the reduced power losses, improved efficiency, and enhanced overall converter performance. The proposed technique is conceptualized, experimentally demonstrating its consequences.

The article is organized starting by the description of the operating principle that govern the converter (section II) allowing the designer to meet the restrictions defined by the specifications: operating ranges of switching frequency, input voltage and output power. The strict height limitation of 13 mm drives the design to a planar core constraining the core geometry and increasing the windings complexity, section III exposes a novel model to achieve symmetric coupling for the planar transformer and inductor, identifying and compensating the effect of the fringing in the magnetic coupling design. In section IV a Pareto-optimization is developed for a constrained design space limited by technological limitations (materials), manufacturing process (core geometry) and application-specific features (converter maximum height). Ultimately, a demonstrator will be built (section V) and the experimental results for 1 kW are given in section VI with section VII concluding the work.

II. Theoretical Analysis

A. Operating principle

The simplified schematic of the proposed Three-Phase LLC converter based on the wye-delta transformer is shown in Fig. 1. Both the inverter and rectifier operate with three 50 % duty cycle PWM signals (1 for each leg) 120° apart.

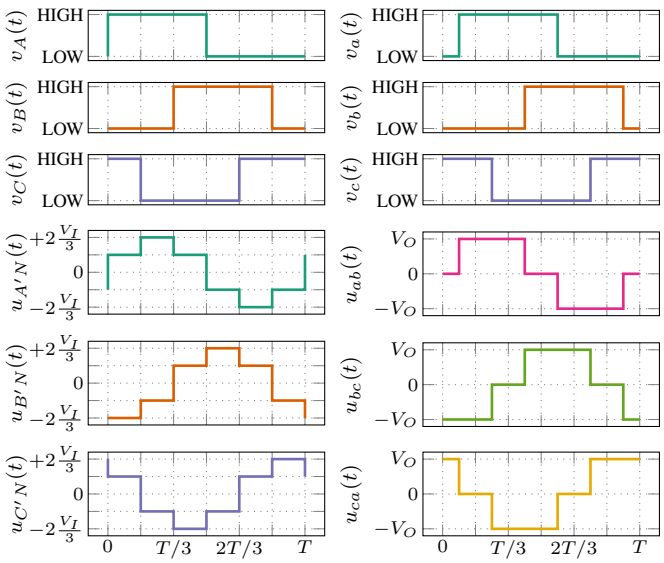

(a) Inverter switching to neutral (b) Rectifier into the secondary

Fig. 2: Voltages seen by the inverter and rectifier (at resonance)

The circuit behaviour is completely defined once we have chosen the gate voltage at each and every one of the switches and its steady-state can be known.

The sum of the currents for the three primaries and three secondaries null each other,

$$i_A(t) + i_B(t) + i_C(t) = 0 \tag{1a}$$

$$i_a(t) + i_b(t) + i_c(t) = 0 \tag{1b}$$

from (1), we can conclude that the voltage across the resonant tank in the time-domain is given by the sum of the voltages across the capacitors C_r,

$$\sum_k v_{C_r,k} = \sum_k \int_0^t \frac{i_{L_r,k}(\tau)}{C_r} \mathrm{d}\tau = 0 \tag{2a}$$

and the sum of voltages across the inductors L_r,

$$\sum_k v_{L_r,k} = \sum_k L_r \frac{\mathrm{d}i_{L_r,k}(t)}{\mathrm{d}t} = 0 \tag{2b}$$

taking the neutral point of the star as the reference point, we can calculate the voltage across the resonant tank and primary of each phase v_{kN},

$$\left.\begin{aligned} v_A - v_B &= v_{AN} - v_{BN} \\ v_B - v_C &= v_{BN} - v_{CN} \\ v_C - v_A &= v_{CN} - v_{AN} \\ v_{AN} + v_{BN} + v_{CN} &= 0 \end{aligned}\right\} v_{kN} = \frac{2v_k - \sum_{j\neq k} v_j}{3} \tag{3}$$

The rectified voltages are trivial to calculate as the voltage at the output is forced by the rectifier, obtaining the phase voltages at the primaries as the voltage seen by their corresponding secondaries multiplied by the winding turns ratio (Fig. 2).

In Fig. 2 it is assumed that the converter operates at resonance and, consequently, the fundamental harmonic of the voltages from each switching node to the neutral on the primary and the voltage reflected from the secondary are in phase.

When this is happening, a phase delay of $\Delta\varphi = 30°$ between the gate signals at the primary and the secondary side is present. This delay in the gate pulses (between v_k and v_K in Fig. 3) is due to the nature of the wye-delta transformer (30° phase-shift transformer).

When the converter is operating out of resonance, an additional phase delay between the inverter and rectifier has to be performed to mimick the behaviour of an ideal diode. Fig. 3 shows the two most relevant cases for inductive and capacitive behaviour. In principle, six regions can be differentiated (three inductive $\Delta\varphi \in (0°, 180°]$ and three capacitive $\Delta\varphi \in (-180°, 0°]$) but in normal operation, only the first two inductive regions ($\Delta\varphi \in (0°, 120°]$) are relevant as the third only applies at low power and high-frequency (non-narrow frequency range operation), while the capacitive defines the frontier between ZVS and ZCS operation.

The transformer model used in further analysis is shown in Fig. 4. Where a very low leakage inductance is considered (unity coupling factor between primaries and secondaries).

The voltage across the secondaries $u_{ab}(t)$, $u_{bc}(t)$ and $u_{ca}(t)$ induces a magnetic flux $v_{ij} = \mathrm{d}\Phi_{ij}/\mathrm{d}t$ on each phase of the transformer. According to the volt-second product of the core shown in u_{ab} (Fig. 6), the peak of the B-field is given by

$$\Phi_{ij} = \int v_{ij}(t)\mathrm{d}t \rightarrow V_O = \frac{\hat{B} n_s A_e}{T_S/6} \longrightarrow \hat{B} = \frac{V_O}{6 f_S n_s A_e} \quad (4)$$

the same procedure can be repeated for the single phase LLC, this time, with half the period of volt-second product,

$$\Phi_{ij} = \int v_{ij}(t)\mathrm{d}t \rightarrow V_O = \frac{\hat{B} n_s A_e}{T_S/4} \longrightarrow \hat{B} = \frac{V_O}{4 f_S n_s A_e} \quad (5)$$

meaning that the B-field on the three-phase transformer core is 33 % lower by evaluating the relationship between (4) and (5) than the single-phase LLC for the same transformer effective area A_e, output voltage V_O and switching frequency f_S, providing us means to decrease the volume of the transformer.

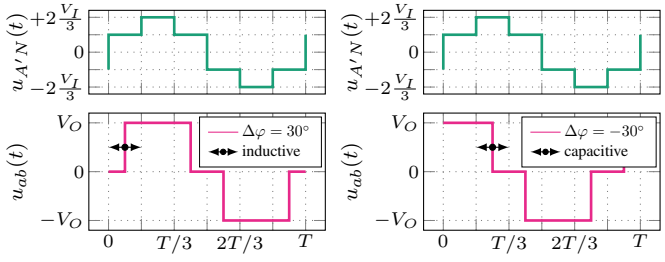

(a) Inductive behaviour (b) Capacitive behaviour

Fig. 3: Voltages at both sides of the resonant tank refered to the neutral of the primary for different load types (inductive and capacitive)

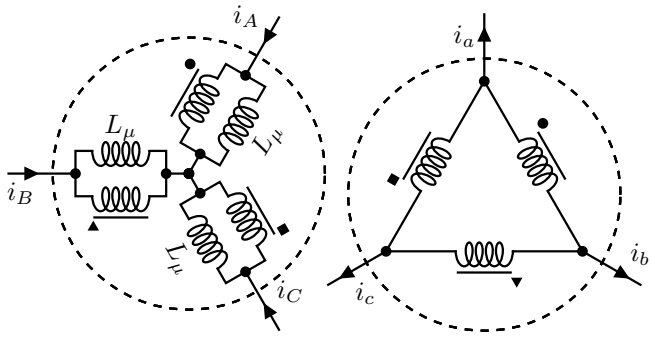

(a) Primary in wye configuration (b) Secondary in delta configuration

Fig. 4: Three-Phase transformer model with magnetizing inductance refered to the primary

Usually, the output capacitance C_L is big enough so that at maximum output can be considered constant in steady-state. Once the switching frequency, f_S, and the output voltage V_O are set, and the gain required given that the input voltage V_I is within the possible range of gains, the inverter-rectifier delay $\Delta\varphi$ has an unique inductive solution ($\Delta\varphi > 0°$) and thus the steady-state solution can be found according to the solution of the differential equation of the resonant tank [21],

$$i_{L_r,A}(t) = \frac{c_1}{Z_r}\sin(\omega_r t) + c_2\cos(\omega_r t) \quad (6a)$$

$$v_{C_r,A}(t) = v_{C_r,A}(0) + c_1\left[1 - \cos(\omega_r t)\right] + Z_r c_2 \sin(\omega_r t) \quad (6b)$$

$$v_{L_\mu,A}(t) = v_{L_\mu,A}(0) + n\int_0^t \frac{u_{ab}(t)}{L_\mu}\,\mathrm{d}t \quad (6c)$$

where constants c_1 and c_2 are the initial voltage across the inductor and the initial current through the inductor respectively,

$$c_1 = V_I - v_{C_r,A}(0) - n u_{ab}(0) \quad (7a)$$

$$c_2 = i_{L_r,A}(0) \quad (7b)$$

The exact solution is obtained by ensuring the output current $i_O(t)$ continuous (C^0). This means that the switching patterns at the secondary match the behaviour of an ideal diode. The topology is driven by the switching frequency of the bridges and the delay between them to compensate for the input voltage and accomplish soft-switching in the secondary. Imposing $+V_O$ across the winding ij when $i_i > i_{k\neq i}$ and $-V_O$ when $i_i < i_{k\neq i}$ (see Fig. 6).

The average output current is given by the integral of the six-pulse rectification,

$$\frac{\hat{I}_O}{I_O} = \frac{1}{T/6}\int_{-\frac{T}{12}}^{\frac{T}{12}} \cos\left(2\pi\frac{t}{T}\right)\,\mathrm{d}t = \frac{3}{\pi} \quad (8)$$

The input current from the DC power supply is also a six-pulse current waveform. This means that the current stress of the input filter is dramatically improved from the single-phase LLC as only the harmonics multiple of six have to filtered out.

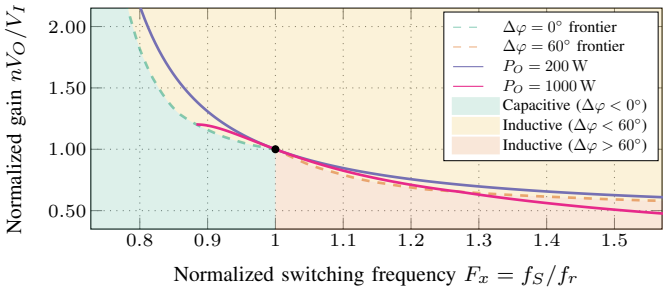

Fig. 5: Resonant tank characteristical gain as function of the normalized switching frequency F_x

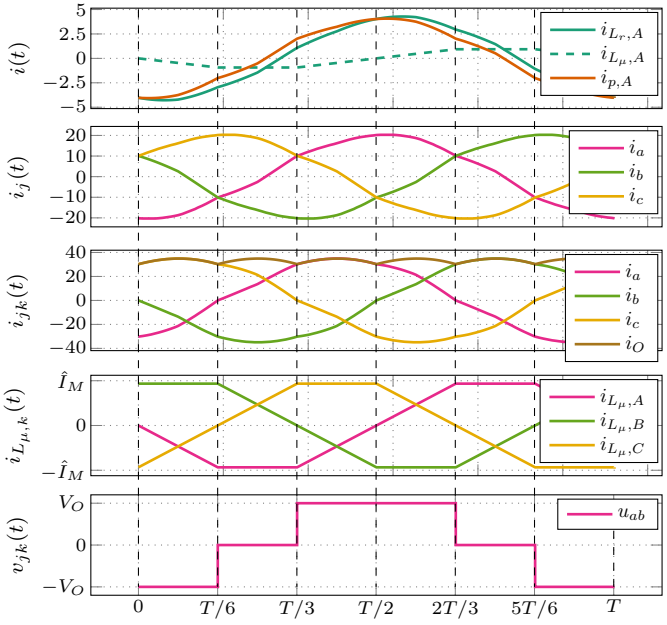

Fig. 6: Six-pulse three-phase rectifier behaviour

B. Resonant tank gain

The topology behaves as a DC transformer (load independent) at resonance, this means that the reactive power is solely given by the magnetizing inductance of the transformer.

The operation out of resonance is required to fix the gain of the resonant tank and compensate the variation on the input voltage. This affects the reactive power in a way that frequencies above resonance will inductively load the input and capacitively under resonance.

Fig. 5 shows the exact resonant tank characteristical gain against the switching frequency according to (6).

C. Fundamental-Harmonic Approximation

The analysis of LLC converters is typically started with the fundamental-harmonic approximation (FHA) as it provides a straightforward method to describe the converter gain as a function of the switching frequency [22].

This process is well-documented in the literature for the single-phase LLC but it is usually summarized in the expression

$$\frac{nV_O}{V_I} = \frac{(m-1)\cdot F_x^2}{\sqrt{\left(mF_x^2-1\right)^2 + Q^2(m-1)^2F_x^2\cdot\left(F_x^2-1\right)^2}} \tag{9}$$

where the L_r, C_r and L_μ design space is transformed into the Z_r, m, Q being the total inductance to resonant inductance ratio $m = 1+L_\mu/L_r$, F_x the normalized switching frequency, $Q = Z_r/R_{eq}$ the quality factor and the equivalent AC resistance reflected to the primary $R_{eq} = 8n^2/\pi^2 R_L$. Fig. 7 shows the equivalent FHA circuit for the three-phase LLC converter in wye-delta. As the power transmitted is split between the three phases, a single-phase FHA equivalent circuit is proposed.

The complete process though is obtained from the impedance representation at the operating frequency f_S (fundamental-harmonic) for which

$$\left.\begin{aligned}\bar{z}_r &= \mathrm{j}\omega_o L_r + \frac{1}{\mathrm{j}\omega_o C_r}\\ \bar{z}_o &= \mathrm{j}\omega_o L_\mu \| R_{eq}\end{aligned}\right\} \bar{U}_o = \frac{\bar{z}_o}{\bar{z}_o+\bar{z}_r}\cdot\bar{U}_i \tag{10}$$

where the real time-domain spectrum of $\bar{U}_i$ and $\bar{U}_o$ is known (given by Fourier's expansion)

$$\bar{U}_i = a_0 + \mathrm{j}b_0 \tag{11}$$

For synchronous rectification, both voltages are square waveforms meaning that the magnitude of $\bar{U}_o$ must be multiplied by $\pi/(4n)$ to obtain V_O.

The same process can be repeated calculating the amplitude of the first harmonic of $v_{k'N}(t)$ as the input voltage

$$R_{eq,\mathrm{Y}\Delta} = 9\left(\frac{3}{\pi}\right)^2\cdot n^2 R_L \tag{12a}$$

$$\frac{V_O}{|\bar{U}_o|} = \frac{2}{\pi}\sqrt{3} \tag{12b}$$

D. Output capacitance selection

An initial approximation (for low ripple) on the voltage ripple is obtained by the integration of the difference of the input current from the rectifier and the output current to the

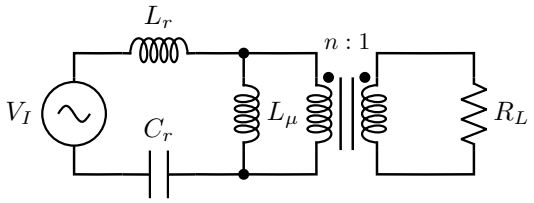

Fig. 7: Single-phase equivalent circuit (FHA) for a Three-Phase LLC converter in wye-delta

load when the former is higher than its average value, defining $a = \hat{I}_O / I_O$

$$\Delta v_O(a) = \frac{I_O}{\omega C_O} \int_{\sin^{-1}(a)}^{\pi - \sin^{-1}(a)} \sin(\omega_{min} t)\, \mathrm{d}(\omega t) = \\ = \frac{I_O}{\omega C_O} \left[2a \tan^{-1}\left(\frac{a}{\sqrt{1-a^2}} \right) + 2\sqrt{1-a^2} - a \cdot \pi \right] \quad (13)$$

where a is calculated averaging the input current to the capacitor as in (8) for the six-pulse rectification, which for the single-phase LLC $a = 2/\pi$ while for the three-phase LLC, $a = 3/\pi$. Evaluating on (13), we get that for the same output voltage ripple, the three-phase LLC requires less than a 38.5 % of what the single-phase LLC requires.

For the worst case full power output (1 kW) as specified in table II, minimum switching frequency (810 kHz) and 1 % voltage ripple (100 mV), 2 µF are needed. We selected 21 MLCC 100 nF capacitors in parallel, to achieve this capacitance (*CGA5L2C0G1H104J160AE*).

E. Design rules of the components

Every parameters of the converter has a big impact in the design. To unveil this entanglement, a design guideline is explained in this subsection with the purpose of clarifying the procedure. The biggest contribution of each parameter is listed,

- Transformer winding turns ratio n: defines the voltage gain at resonance, due to the wide input voltage gain required, it is desirable that operates in both step-down (above resonance) and step-up (below resonance)
- Resonant inductance L_r: contributes to the quality factor of the tank $Q = \omega L_r / R_{eq}$ and thus its selectivity
- Resonant capacitance C_r : defines the resonant frequency of the tank and must be able to withstand the voltage across it due to the resonant current
- Magnetizing inductance L_μ: defines the sensitivity of the gain, including the maximum boost of the LLC

To calculate the current and voltage rating of the resonant tank it can be assumed that the resonant current is dominant over the magnetizing, through (8), its peak is given by

$$\hat{I}_{L_r} = \frac{\pi}{3\sqrt{3}} \frac{1}{n} \frac{P_O}{V_O} \quad (14a)$$

and the voltage across the resonant capacitor,

$$\hat{V}_{C_r} = \frac{\hat{I}_{L_r}}{2\pi f_{min} C_r} \quad (14b)$$

The first step is to choose the winding turns ratio n which, when selecting a single-turn secondary due to the high amplitude current on the secondary side, $n = 5$ is the only integer that centres the resonance within the gain range calculated from the input voltage range in normal operation.

For a first iteration of the converter and as a proof-of-concept, the maximum voltage across the capacitor was selected to 230 V, meaning that for a resonant frequency $f_r = 900$ kHz, the value for the resonant capacitor is $C_r = 3.32$ nF and thus, $L_r = 9.6$ µH.

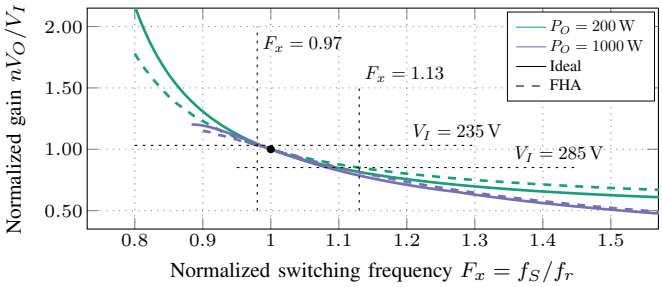

Fig. 8: Ideal and FHA characteristical gain of the converter

TABLE III: Design made to comply with the specifications

Parameter	Value	Description
L_r	9.6 µH	Inductance of the resonant tank
C_r	3.32 nF	Capacitance of the resonant tank
L_μ	12.0 µH	Magnetizing inductance
C_L	2 µF	Output capacitance
n_1	5	Number of turns of the primary
n_2	1	Number of turns of the secondary
Q_i	GS66508T	Inverter transistor
Q_r	BSZ018N04LS6	Rectifier transistor

With both $Z_r = \sqrt{L_r/C_r}$ and f_r decided, it only exists a single value of m that is capable of meeting the requirement of $\Delta F_x = 10\,\%$ for the input voltage and output power ranges. In this case, $m = 2.27$ making $L_\mu = 12$ µH.

The parameters of the topology were designed considering the maximum and minimum gains, as once ΔF_x is set for an input voltage and output power range, only one set of values for L_r, C_r and L_μ is obtained. These gains are derived from table II with (9) obtaining the response in Fig. 8. The designed values are listed in table III.

III. Magnetic Design

Unlike the resonant capacitor which voltage and current ratings as well as its capacitance are known and can be found in a parametric search, the design and optimization of L_r and L_μ requires a lot of calculation and simulation effort, even though that the nominal lumped-model values are known.

Within the behaviour of three-phase magnetics, and more predominantly, in planar magnetics, the potential for phase unbalance increases. These phenomenon impacts significantly the performance of power converters, requiring the development of compensation techniques to mitigate their effects.

This phenomenon manifests as voltage and current dependance between phases. When the synchronous rectifier forces the voltage across the secondary windings, if unbalanced, results in an uneven storage of magnetizing energy among the phases. Consequently, an unbalance becomes apparent during operation, nonetheless, the issue worsens in a three-phase inductor for the same unbalance, rather than the transformer itself. This is due to an additional series coupling between two phases. For instance, the current flowing through phase k will induce an additional series voltage in the other phases, which

are 120 degrees apart from phase k, unbalancing the system.

This is because of the non-symmetry of the typical three-phase magnetic core (three equal columns in a EE core), where one of the columns (central) presents a shorter magnetic path length to the three columns merging point compared with the other columns (laterals). To overcome this, in this section, a comprehensive analysis is made to address non-symmetrical magnetic core structures and achieve optimal performance.

A. Gapped Three-Port Asymmetric Magnetic Core

Three-phase core architectures require to have three independent magnetic paths, and this is translated into an architecture with three winding positions usually refered to as three ports.

In general, it is desirable that balanced three-phase magnetic components are built upon symmetric structures such as delta or wye cores [23]. Nonetheless, these constructions have higher volume and unconvenient terminations for the windings in a linear downstream circuit topology.

The utilization of non-symmetrical magnetic core structures leads to non-compensated magnetic component, this fact is relevant as it is detrimental to the balancing of the phases.

In the case of the synchronous three-phase LLC converter, each phase has its current shifted, unbalancing the soft-switching of the inverter (different switching currents on the three-phase bridge leading to loss of ZVS) and the currents in the secondary (risk of losing its quasi-ZCS). Altogether, a symmetric magnetic component in a three-phase system contributes to the minimization of the unbalance between phases, ultimately reducing the power losses and thus, improving its thermal stability.

In [18], a three-column EE-core was built with two different soft materials in order to compensate the magnetic coupling between columns. The same effect can be accomplished by narrowing the central column respect to the laterals as the equivalent reluctance seen from the null flux singular point of the core is compensated.

In this subsection, the geometry compensation is derived for two three-port core geometries: the EE-core and the EI-core, an alternative approach is developed in appendix A. The core dimensioning is shown in Fig. 9.

The mathematical analysis is performed based on the magnetostatic problem for which Ampère's Law (15) and the

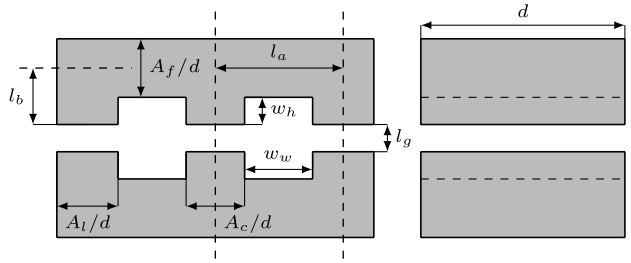

(a) Front view (b) Side view

Fig. 9: EE-core dimensioning

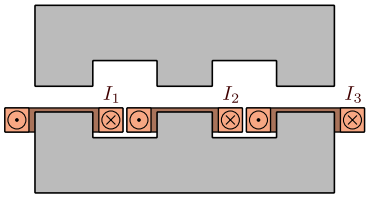

Fig. 10: Winding layout

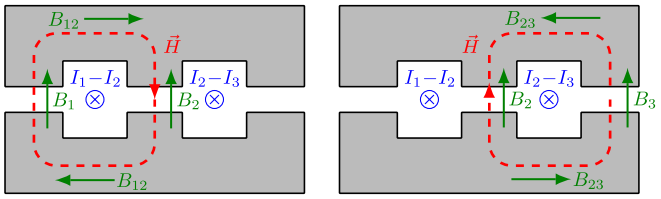

(a) Left current loop (b) Right current loop

Fig. 11: Definition of the signs of the H-field and the current through the window

Magnetic Flux Conservation Law (16) are used,

$$\oint_L H \ \mathrm{d}l = \iint_S J \ \mathrm{d}S \tag{15}$$

$$\iint_S B \ dS = 0 \tag{16}$$

all the analysis are made considering the fringing with σ_l and σ_c correction factors, reserved for future analysis in this subsection.

To simplify the analysis and make it more comprehensible, an approach regarding the winding layout in this section was adopted. Instead of detailing the winding layout for each individual phase, the winding arrangement was considered as one phase for each column. Fig. 10 provides a visual representation of this simplified winding layout, illustrating how we treated the windings as a single phase within each column, highlighting the connections and relationships that are relevant to our analysis and design.

Evaluating the H-loops defined in Fig. 11 with (15) we obtain the first two equations,

$$\left(\frac{l_g}{\sigma_l}+\frac{2l_b}{\mu_r}\right)\frac{B_1}{\mu_0}+\frac{2l_a}{\mu_r}\frac{B_{12}}{\mu_0}-\left(\frac{l_g}{\sigma_c}+\frac{2l_b}{\mu_r}\right)\frac{B_2}{\mu_0}=I_1-I_2 \tag{17}$$

$$\left(\frac{l_g}{\sigma_l}+\frac{2l_b}{\mu_r}\right)\frac{B_3}{\mu_0}+\frac{2l_a}{\mu_r}\frac{B_{23}}{\mu_0}-\left(\frac{l_g}{\sigma_c}+\frac{2l_b}{\mu_r}\right)\frac{B_2}{\mu_0}=I_2-I_3 \tag{18}$$

to complete the system, we apply (16) to the junction magnetic paths between columns,

$$B_{12}=B_1\cdot\frac{A_l}{A_f} \tag{19a}$$

$$B_{23}=B_3\cdot\frac{A_l}{A_f} \tag{19b}$$

and to the singular spot where the three magnetic fluxes of the columns meet,

$$B_1\cdot A_l+B_2\cdot A_c+B_3\cdot A_l=0 \tag{19c}$$

Equation (19) can be substituted into (17) and (18) and together with (19c), a system of three linear equations with B_1, B_2 and B_3 (B-field for each column) is defined,

$$\mathbf{Ax} = \mathbf{b} \longrightarrow \mathbf{x} = \mathbf{A}^{-1} \cdot \mathbf{b} \tag{20a}$$

$$\begin{cases} a_{11} = \dfrac{1}{\mu_0}\left[\dfrac{l_g}{\sigma_l} + \dfrac{2l_b}{\mu_r} + \dfrac{2l_a}{\mu_r}\dfrac{A_l}{A_f}\right] \\ a_{23} = a_{11} \\ a_{12} = \dfrac{l_g}{\sigma_c} + \dfrac{2l_b}{\mu_r} \\ a_{22} = a_{12} \end{cases} \tag{20b}$$

$$\mathbf{A} = \begin{bmatrix} a_{11} & a_{12} & 0 \\ 0 & a_{22} & a_{23} \\ A_l & A_c & A_l \end{bmatrix}, \ \mathbf{x} = \begin{bmatrix} B_1 \\ B_2 \\ B_3 \end{bmatrix}, \ \mathbf{b} = \begin{bmatrix} I_1 - I_2 \\ I_2 - I_3 \\ 0 \end{bmatrix} \tag{20c}$$

The B-field now is completely defined and solved with (20a). To fill the inductance matrix $\mathbf{L}$ of (21) for a three-column, single-turn magnetic component we define the flux on each column j (ϕ_{ij}) and divide it by the current I_i that causes it obtaining (22).

$$\mathbf{L}_t = \begin{bmatrix} L_{ll} & M_{lc} & M_{ll} \\ M_{lc} & L_{cc} & M_{lc} \\ M_{ll} & M_{lc} & L_{ll} \end{bmatrix} \tag{21}$$

$$L_{ll} = \left.\frac{\phi_1}{I_1}\right|_{\substack{I_2 = 0 \\ I_3 = 0}} \approx +\mu_0 \frac{A_l(A_c + A_l)}{l_g(2A_l + A_c)} \tag{22a}$$

$$L_{cc} = \left.\frac{\phi_2}{I_2}\right|_{\substack{I_1 = 0 \\ I_3 = 0}} \approx +\mu_0 \frac{2A_cA_l}{l_g(2A_l + A_c)} \tag{22b}$$

$$M_{ll} = \left.\frac{\phi_1}{I_3}\right|_{\substack{I_2 = 0 \\ I_3 = 0}} \approx -\mu_0 \frac{A_l^2}{l_g(2A_l + A_c)} \tag{22c}$$

$$M_{lc} = \left.\frac{\phi_1}{I_2}\right|_{\substack{I_1 = 0 \\ I_3 = 0}} \approx -\mu_0 \frac{A_cA_l}{l_g(2A_l + A_c)} \tag{22d}$$

This approximation represents the effect of an ideal magnetic core ($\mu_r \to +\infty$). The complete solution to (20a) can be solved to get $M_{lc} = M_{ll}$, for which the lateral column must shrink in the quantity:

$$A_l^* = A_c \cdot \frac{A_f\left(2\dfrac{l_b}{\mu_c} + \dfrac{l_g}{\sigma_l}\right)}{A_f\left(2\dfrac{l_b}{\mu_c} + \dfrac{l_g}{\sigma_c}\right) - 2A_c\dfrac{l_a}{\mu_c}} \tag{23}$$

where a minimum air-gap length is required extracted from nulling of the denominator of (23),

$$l_g \geq \sigma_c \cdot \frac{2}{\mu_r}\left(\frac{A_c}{A_f}l_a - l_b\right) \tag{24}$$

When (23) is satisfied, we can calculate the exact solution for (22):

$$L_{ll} = \left.\frac{\phi_1}{I_1}\right|_{\substack{I_2 = 0 \\ I_3 = 0 \\ A_l = A_l^*}} = +\mu_0 \frac{2}{3}\frac{A_c}{\dfrac{l_g}{\sigma_c} + \dfrac{2l_b}{\mu_c}} \tag{25a}$$

$$L_{cc} = \left.\frac{\phi_2}{I_2}\right|_{\substack{I_1 = 0 \\ I_3 = 0 \\ A_l = A_l^*}} = +\mu_0 \frac{2}{3}\frac{A_c}{\dfrac{l_g}{\sigma_c} + \dfrac{2l_b}{\mu_c}} \tag{25b}$$

$$M_{ll} = \left.\frac{\phi_1}{I_3}\right|_{\substack{I_2 = 0 \\ I_3 = 0 \\ A_l = A_l^*}} = -\mu_0 \frac{1}{3}\frac{A_c}{\dfrac{l_g}{\sigma_c} + \dfrac{2l_b}{\mu_c}} \tag{25c}$$

$$M_{lc} = \left.\frac{\phi_1}{I_2}\right|_{\substack{I_1 = 0 \\ I_3 = 0 \\ A_l = A_l^*}} = -\mu_0 \frac{1}{3}\frac{A_c}{\dfrac{l_g}{\sigma_c} + \dfrac{2l_b}{\mu_c}} \tag{25d}$$

An accurate representation of the air-gap effect in the coupling of the windings is essential when designing the components. For such task, two correction factors were introduced previously into the analysis made in the present paper denoted by σ_l and σ_c for the lateral and central columns respectively.

In [24], a simplified method for calculating the reluctance of the air-gap was described based on the Schwarz-Christoffel transformation for infinitely long magnetic cores (2-D). A similar approach was taken in [25] were the afore-mentioned work is extrapolated into both directions of the cross-section of the air-gap. Applying it into our problem we get the correction factor of the effective air-gap in the central column,

$$\sigma_{xc} = \frac{a_c \cdot \pi}{a_c \cdot \pi + 2l_g \cdot \left(1 + \ln\left(\pi\dfrac{2l_b - a_f}{4l_g}\right)\right)} \tag{26a}$$

$$\sigma_{yc} = \frac{d \cdot \pi}{d \cdot \pi + 2l_g \cdot \left(1 + \ln\left(\pi\dfrac{2l_b + a_f}{4l_g}\right)\right)} \tag{26b}$$

$$\sigma_c = \sigma_{xc} \cdot \sigma_{yc} \tag{26c}$$

and in the lateral columns,

$$\sigma_{xl} = \frac{a_l \cdot \pi}{a_l \cdot \pi + 2l_g \cdot \left(1 + \ln\left(\pi\dfrac{2l_b - a_f}{4l_g}\right)\right)} \tag{27a}$$

$$\sigma_{yl} = \frac{d \cdot \pi}{d \cdot \pi + 2l_g \cdot \left(1 + \ln\left(\pi\dfrac{2l_b + a_f}{4l_g}\right)\right)} \tag{27b}$$

$$\sigma_l = \sigma_{xl} \cdot \sigma_{yl} \tag{27c}$$

Fig. 12 shows the comparison between the mutual inductances M_{lc} and M_{ll}. The application of this expression leads to a 5 % maximum error without compensating for the fringing effect.

Once the methodology to compensate the asymmetry of a planar EE core is established and including the effect of the fringing in the coupling, the geometry dimensioning (equation (25)) is validated via finite-element simulation. The simulations were performed in Maxwell 3D with minimal track width to discard the effect of the inductance added by the windings.

The results are represented in Fig. 12, the mutual inductances M_{ll} and M_{lc} shows that M_{lc} does not significantly depend on the size of the lateral column A_l, while M_{ll} varies up to a 15 %, reducing the maximum error to a 7.5 %. These cases can be observed when comparing $\sigma = f(A_l^*)$ (fringing

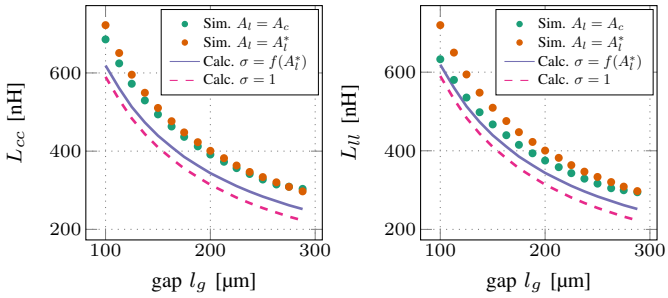

(a) Central self-inductance L_{cc} (b) Lateral self-inductance L_{ll}

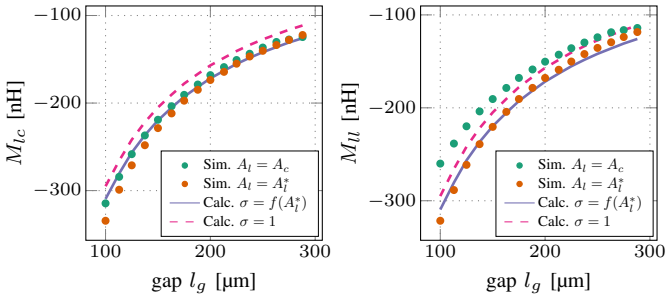

(c) Lateral-central M_{lc} (d) Lateral-lateral M_{ll}

Fig. 12: Comparison of the inductance matrix components calculated with (23) and the obtained in a magnetostatic ANSYS simulation sweeping $A_l^* = f(l_g)$ and $A_l = A_c$

effect considered) with the simulated results $A_l = A_l^*$, demonstrating the predictability of the proposed model. With it, the transformer and resonant inductor designs can proceed.

1) Wye-Delta Transformer: A single-phase transformer can be represented as the quadripole given by (28) with $\mathbf{u} = \mathbf{Z}_{1\phi} \cdot \mathbf{i}$.

$$\mathbf{Z}_{1\phi} = \begin{bmatrix} \bar{z}_{pp} & \bar{z}_{ps} \\ \bar{z}_{sp} & \bar{z}_{ss} \end{bmatrix} \tag{28}$$

In general, a three-phase transformer, is electrically analyzed by assuming it to be balanced (equivalent to a single-phase). No matter how the windings are coupled (Fig. 13), we can define a 6×6 matrix for the six windings (3 primaries and 3 secondaries),

$$\mathbf{Z}_{6\mu} = \begin{bmatrix} \mathbf{Z}_{AA} & \mathbf{Z}_{AB} & \mathbf{Z}_{AC} \\ \mathbf{Z}_{BA} & \mathbf{Z}_{BB} & \mathbf{Z}_{BC} \\ \mathbf{Z}_{CA} & \mathbf{Z}_{CB} & \mathbf{Z}_{CC} \end{bmatrix}, \ \mathbf{Z}_{jk} = \begin{bmatrix} \bar{z}_{p_j p_k} & \bar{z}_{p_j s_k} \\ \bar{z}_{s_j p_k} & \bar{z}_{s_j s_k} \end{bmatrix} \tag{29a}$$

$$\mathbf{u} = \begin{bmatrix} \mathbf{u}_A & \mathbf{u}_B & \mathbf{u}_B \end{bmatrix}^T = \\ = \begin{bmatrix} \bar{U}_A & \bar{U}_a & \bar{U}_B & \bar{U}_b & \bar{U}_C & \bar{U}_c \end{bmatrix}^T \tag{29b}$$

$$\mathbf{i} = \begin{bmatrix} \mathbf{i}_A & \mathbf{i}_B & \mathbf{i}_C \end{bmatrix}^T = \\ = \begin{bmatrix} \bar{I}_A & \bar{I}_a & \bar{I}_B & \bar{I}_b & \bar{I}_C & \bar{I}_c \end{bmatrix}^T \tag{29c}$$

$$\mathbf{u} = \mathbf{Z}_{6\mu} \cdot \mathbf{i} \tag{29d}$$

equivalent to a block matrix composed by the merge of the three pairs of primaries and secondaries. In order for $\mathbf{Z}_{6\mu}$ to behave as three independent single-phase transformers, an

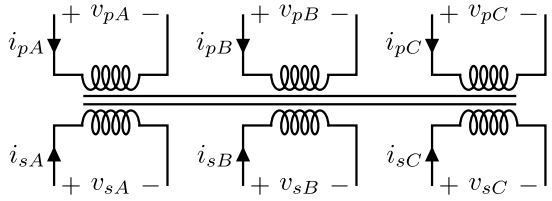

Fig. 13: Six arbitrarily coupled inductors

equivalent matrix has to be found so that only the main diagonal is filled while null matrices $\mathbf{O}_{2\times2}$ fill the rest.

$$\mathbf{Z}_{3\phi} = \begin{bmatrix} \mathbf{Z}_{AA}^* & \mathbf{O}_{2\times2} & \mathbf{O}_{2\times2} \\ \mathbf{O}_{2\times2} & \mathbf{Z}_{BB}^* & \mathbf{O}_{2\times2} \\ \mathbf{O}_{2\times2} & \mathbf{O}_{2\times2} & \mathbf{Z}_{CC}^* \end{bmatrix} \tag{30}$$

If it is assumed that the primary and the secondary windings are perfectly coupled (no leakage), then the equivalent circuit can be represented as shown in Fig. 4.

The condition that we need is that the sum of the currents for the three primaries or three secondaries null each other (Kirchhoff's current law), this is (31).

$$\mathbf{i}_A + \mathbf{i}_B + \mathbf{i}_C = \begin{bmatrix} 0 \\ 0 \end{bmatrix} \begin{cases} \bar{I}_A + \bar{I}_B + \bar{I}_C = 0 \\ \bar{I}_{A'} + \bar{I}_{B'} + \bar{I}_{C'} = 0 \end{cases} \tag{31}$$

If we assume that (30) will be satisfied within the definition of (29d) then we can split the block matrix $\mathbf{Z}_{6\mu}$ into two

$$\mathbf{Z}_{6\mu} = \begin{bmatrix} \mathbf{Z}_{AA} & \mathbf{O}_{2\times2} & \mathbf{O}_{2\times2} \\ \mathbf{O}_{2\times2} & \mathbf{Z}_{BB} & \mathbf{O}_{2\times2} \\ \mathbf{O}_{2\times2} & \mathbf{O}_{2\times2} & \mathbf{Z}_{CC} \end{bmatrix} + \\ + \begin{bmatrix} \mathbf{O}_{2\times2} & \mathbf{Z}_{AB} & \mathbf{Z}_{AC} \\ \mathbf{Z}_{BA} & \mathbf{O}_{2\times2} & \mathbf{Z}_{BC} \\ \mathbf{Z}_{CA} & \mathbf{Z}_{CB} & \mathbf{O}_{2\times2} \end{bmatrix} \tag{32}$$

it is trivial that $\mathbf{Z}_{ij} = \mathbf{Z}_{ji}$ and can be demonstrated that, due to the axial symmetry of an EE or an EI core, $\mathbf{Z}_{AB} = \mathbf{Z}_{CB}$ as the mutual inductance between the central column B and each of the two lateral columns (A and C) is the same. This leads us to the reduction of the last equation to a lateral-to-lateral mutual block matrix $\mathbf{Z}_{ll}$ and to a lateral-to-central block matrix $\mathbf{Z}_{lc}$, we can define a block matrix $\Delta\mathbf{Z} = \mathbf{Z}_{ll} - \mathbf{Z}_{lc}$ so that previous equation is simplified to

$$\mathbf{Z}_{6\mu} = \begin{bmatrix} \mathbf{Z}_{AA} & \mathbf{O}_{2\times2} & \mathbf{O}_{2\times2} \\ \mathbf{O}_{2\times2} & \mathbf{Z}_{BB} & \mathbf{O}_{2\times2} \\ \mathbf{O}_{2\times2} & \mathbf{O}_{2\times2} & \mathbf{Z}_{CC} \end{bmatrix} + \\ + \underbrace{\begin{bmatrix} \mathbf{Z}_{lc} & \mathbf{Z}_{lc} & \mathbf{Z}_{lc} \\ \mathbf{Z}_{lc} & \mathbf{Z}_{lc} & \mathbf{Z}_{lc} \\ \mathbf{Z}_{lc} & \mathbf{Z}_{lc} & \mathbf{Z}_{lc} \end{bmatrix}}_{\mathbf{O}_{3\times3}} + \begin{bmatrix} -\mathbf{Z}_{lc} & \mathbf{O}_{2\times2} & \Delta\mathbf{Z} \\ \mathbf{O}_{2\times2} & -\mathbf{Z}_{lc} & \mathbf{O}_{2\times2} \\ \Delta\mathbf{Z} & \mathbf{O}_{2\times2} & -\mathbf{Z}_{lc} \end{bmatrix} \tag{33}$$

due to (31), it is straightforward to demonstrate that the matrix full of $\mathbf{Z}_{lc}$ does not contribute in the voltage $\mathbf{u}$ when (29d) is applied. Also, if we want $\Delta\mathbf{Z} = \mathbf{O}_{2\times2}$, the only option is that the mutual inductance between lateral columns and between a lateral and the central take the same value, which corresponds to a prior solution demonstrated in (23) which it has been previously obtained by the customization of the columns.

Multiplying by the number of turns in the mutual we obtain the complete flux $\psi = n^2 \cdot \phi$, obtaining an equivalent impedance matrix to the single-phase case in (28),

$$\mathbf{Z}^*_{kk} = \mathrm{j}\omega \begin{bmatrix} n_p^2 & n_p n_s \\ n_p n_s & n_s^2 \end{bmatrix} \cdot (L_{ll} - M_{lc}) \tag{34a}$$

$$L^*_\mu = n_p n_s \cdot (L_{ll} - M_{lc}) = \mu_0 \frac{n_p n_s}{\dfrac{l_g}{\sigma_c A_c} + \dfrac{2 l_b}{\mu_c A_c}} \tag{34b}$$

2) Three-Phase Inductor: As previously mentioned, the use of three single-phase resonant inductors, although straightforward, does not take advantage of the features of a three-phase system. A three-phase inductor is designed to merge the three single-phase inductors as shown in Fig. 14. In this section, a brief analysis mimicking the one for the transformer is performed.

The real behaviour of a three-phase inductor is given in Fig. 14b, in order to be equivalent to three single-phase inductors as in Fig. 14a,

$$\mathbf{Z}_{3\phi} = \begin{bmatrix} \bar{z}^*_{AA} & 0 & 0 \\ 0 & \bar{z}^*_{BB} & 0 \\ 0 & 0 & \bar{z}^*_{CC} \end{bmatrix} \tag{35}$$

equivalent to (30) and

$$\mathbf{Z}_{3\mu} = \begin{bmatrix} \bar{z}_{AA} & \bar{z}_{AB} & \bar{z}_{AC} \\ \bar{z}_{BA} & \bar{z}_{BB} & \bar{z}_{BC} \\ \bar{z}_{CA} & \bar{z}_{CB} & \bar{z}_{CC} \end{bmatrix} \tag{36}$$

Equation (31) is still valid as the primary of the transformer is connected to the inductor so defining $\Delta\bar{z} = \bar{z}_{ll} - \bar{z}_{lc}$, we can split the equation above into three

$$\mathbf{Z}_{3\mu} = \begin{bmatrix} \bar{z}_{AA} & 0 & 0 \\ 0 & \bar{z}_{BB} & 0 \\ 0 & 0 & \bar{z}_{CC} \end{bmatrix} + \underbrace{\begin{bmatrix} \bar{z}_{lc} & \bar{z}_{lc} & \bar{z}_{lc} \\ \bar{z}_{lc} & \bar{z}_{lc} & \bar{z}_{lc} \\ \bar{z}_{lc} & \bar{z}_{lc} & \bar{z}_{lc} \end{bmatrix}}_{\mathbf{O}_{3\times 3}} + \begin{bmatrix} -\bar{z}_{lc} & 0 & \Delta\bar{z} \\ 0 & -\bar{z}_{lc} & 0 \\ \Delta\bar{z} & 0 & -\bar{z}_{lc} \end{bmatrix} \tag{37}$$

again, (23) makes $\Delta\bar{z} \equiv 0$ obtaining the equivalent self-inductance for column k,

$$\bar{z}^*_{kk} = \mathrm{j}\omega \cdot n_l^2 \, (L_{ll} - M_{lc}) \tag{38a}$$

$$L^*_r = n_l^2 \, (L_{ll} - M_{lc}) = \mu_0 \frac{n_l^2}{\dfrac{l_g}{\sigma_c A_c} + \dfrac{2 l_b}{\mu_c A_c}} \tag{38b}$$

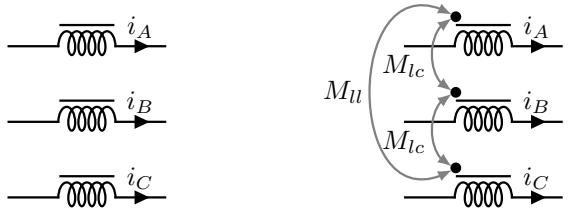

(a) Three single-phase (b) Single three-phase

Fig. 14: Three-Phase coupled inductor electrical model

where n_l is the number of turns of the windings.

B. Core losses

In general, core losses are facilitated as volumetric power losses given by the manufacturer's datasheet. Nonetheless, this data is usually condensed into the Steinmetz Equation (SE),

$$P_V = k \cdot f^\alpha \cdot B^\beta \tag{39}$$

or in the Improved Generalized Steinmetz Equation (IGSE) for non-sinusoidal operation,

$$P_V = \frac{1}{T} \int_0^T k_i \left| \frac{dB}{dt} \right|^\alpha \cdot \Delta B^{\beta-\alpha} \, \mathrm{d}t \tag{40a}$$

$$k_i = \frac{k}{(2\pi)^{\alpha-1} \displaystyle\int_0^{2\pi} |\cos(\theta)|^\alpha 2^{\beta-\alpha} \, \mathrm{d}\theta} \tag{40b}$$

In order to get more accurate representations of the core losses, the data acquisition system used by the MagNet project from Princeton University [26] was used. The material was tested with an arbitrary signal generator to generate a trapezoidal B-field on the material ML91S (see Fig. 15). A curve fitting was performed obtaining $k = 0.320836$, $\alpha = 1.7106$ and $\beta = 3.24364$ for (39).

C. Core geometry

Usually, multiple magnetic parts are used as building blocks to constitute the geometry of the core. In such cases, an unavoidable air-gap is present, moreover, in order to design a balanced three-phase inductor or transformer a minimum gap is mandatory as exposed in (24).

Although a distributed air-gap [27] can reduce local fringing, it leads to higher complexity in the manufacturing of a custom core and reduces the robustness. By simply placing the conductors far away enough from the air-gap for example by using an EI-core instead of EE-core, the fields intersecting the windings decay significantly leading to lower losses.

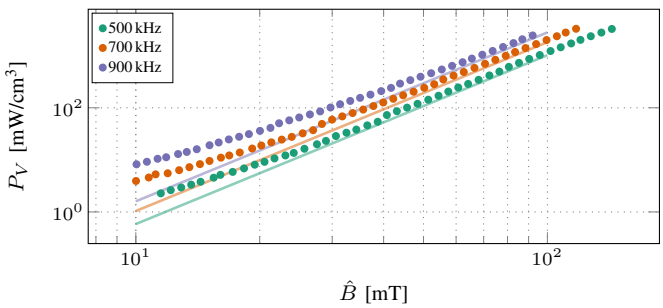

Fig. 15: Experimental power losses measured at 90 °C for a symmetric trapezoidal B-field waveform of $\hat{B}$ peak

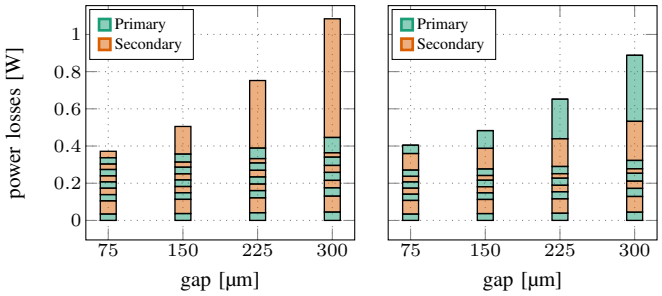

(a) PSPSPSPSPS (b) PSPSPSPSP

Fig. 16: Winding losses for the same EE-core depending on the winding strategy (900 kHz). The bar stack represents the layers of the PCB

D. Winding strategy

For planar magnetic cores in high-frequency applications, the solid wire solution becomes inconvenient as the current stress required in the windings increases in amplitude and harmonic content. The skin effect alone makes the maximum wire diameter to be AWG36 at 1 MHz (127 µm in diameter), requiring a high number of wires in parallel leading into higher proximity and worsening the termination effect [28].

Although Litz wire is a good solution due to its performance at high-frequency, it compromises the economic viability of the converter. PCB windings are less expensive, easily customizable and ideal to create interleaving structures within the winding. For the converter presented, a 5:1 windings turns ratio for the transformer has to be implemented, for which PCB windings are chosen.

In order to make interleaving, the secondary turn is split into 5 to obtain the same current and compensate the increase in the H-field of the primary turns. Nonetheless, due to the asymmetry of this arrangement, this makes it more susceptible to external fields. Instead, the secondary can be split into 4 leaving two primary turns enveloping with the top and bottom layers the rest of the winding turns in the PCB.

With high-frequency currents, skin and proximity effects contribution gain weight in the power losses breakdown. This is especially important in regions of strong magnetic fields (proximity to the air-gap). A set of simulations were run varying the air-gap with a fringing effect close to the top layer of the PCB (Fig. 16). This is made for two strategies (PSPSPSPSPS and PSPSPSPSP). The result depends heavily on the size of the gap and the distance from the winding to it.

Although an initial approximation can be obtained for foil conductors (PCB tracks) with analytical equations [29], fringing losses play a big role in the optimization of the winding losses. Efforts in the fringing power losses estimation are discussed in the literature for planar magnetics [30]. Nonetheless, the highest accuracy is returned by FEM simulations.

E. PCB track losses

Proximity and skin effects in high-current high-frequency designs have a big impact in the losses. For foil conductors (PCB tracks) a set of analytical equations for skin effect is derived in [29],

$$R_{DC} = \frac{\rho_{Cu}}{A_{eq}} l_{eq} \tag{41a}$$

$$\delta = \sqrt{\frac{\rho_{Cu}}{\pi f \mu_{Cu}}} \tag{41b}$$

$$P_{skin} = R_{DC} \cdot F_R \cdot \hat{I}^2 \tag{41c}$$

$$F_R = \frac{\nu}{4} \frac{\sinh(\nu) + \sin(\nu)}{\cosh(\nu) - \cos(\nu)}, \ \nu = \frac{t}{\delta} \tag{41d}$$

being F_R a corrective factor, t the thickness of the copper track (2 oz/ft), δ the skin depth, ρ_{Cu} the resistivity of the copper and μ_{Cu} its absolute magnetic permeability.

Due to the low voltage at the output compared to the input voltage, high-frequency high-currents will be manifest in the rectifier circuit. Higher currents tend to focus on the sides of the track leading to higher RMS current and thus, higher power losses.

Flux cancellation designs such as in [31] are an option when parallelizing many transistors and more PCB layers are available at the cost of producing higher complexity layouts. In the present work, a first prototype was designed with current orthogonality executed as much as possible to minimize the proximity losses.

The purely ohmic loss obtained in a simulation performed in ANSYS with 36 A peak, 900 kHz returned 4.53 W. Evaluating (41) for pieced sections of the conduction path (different l_{eq} and A_{eq}) returned 4.5 W. Testing this experimentally is also possible as three-phase currents can be achieved with the already buit-in resonant tank:

- Short-circuiting the transistors in the inverter and allowing the current to rush-in into the tracks of the rectifier
- Short-circuiting the three output terminals of the secondary windings

in both cases, as in a three-phase system fault, the current will be strictly limited by the impedance of the short-circuit (the impedance of the rectifier board in the first case and the impedance of the windings in the second case). To avoid it, the current at the primary (resonant tank) was kept at a certain value peaking at 4.2 A which will translate into 36 A in the secondary. This way, the primary is stressed in the same way and the power losses of the inverter, resonant tank and transformer can be crossed-out of the equation discriminating the power losses of the rectifier board.

Fig. 17 shows the power losses with the two aforedmentioned experiments, for the primary current at full load, 4.4 W were obtained, defining a 0.5 % of efficiency loss for 1 kW operation.

IV. Pareto-Optimal design

An EE-core was taken as reference to calculate the main design parameter of a three-phase planar transformer. Nonetheless, an EE-core and an EI-core are equivalent so the same equation can be applied by making the equivalence.

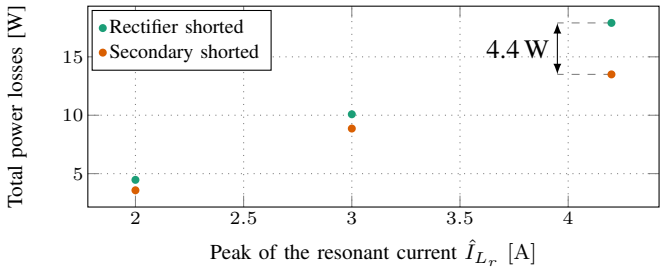

Fig. 17: Experimental PCB power losses as function of a three-phase injected sinusoidal current at 900 kHz

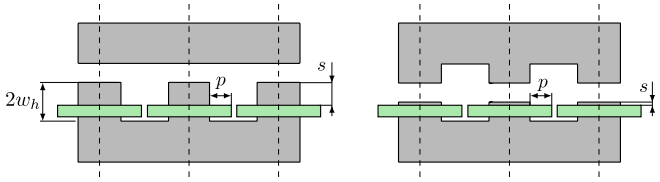

(a) EI-core (b) EE-core

Fig. 18: Extra design space parameters of the design

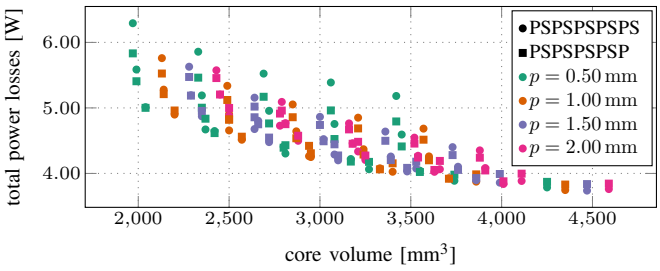

(a) Transformer pareto front

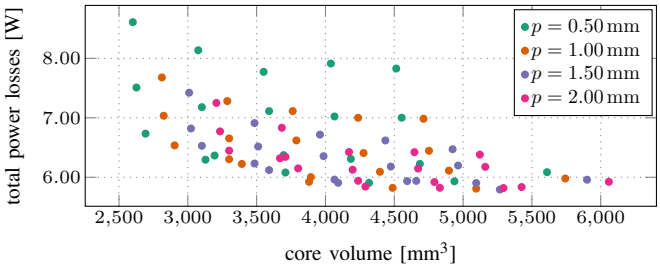

(b) Inductor pareto front

Fig. 19: Pareto-front of the three-phase inductor and three-phase transformer with an EE-core

A. Design space

As it's a height-constrained core ($h = 12.9\,\mathrm{mm}$), we can show from Fig. 9 that the design has 6 degrees of freedom that have to be defined,

- Depth of the core d
- Width of the window w_w
- Half the height of the window w_h
- Area of the central column $A_c = a_c \cdot d$
- Area of the lateral column $A_l = a_l \cdot d$
- Air-gap length l_g

we can then discuss the mandatory constrains of the design:

- Central column shrinkage: (23) shows the relationship between the lateral and central columns as funcion of l_g.
- Thermal dissipation capabilities: this will define the maximum allowed B-field in the column through the power losses of the core. Estimating it can be tricky as accurate models (simulations) sheltered by experimental tests have to be performed being 500 mW/cm^3 is a good starting point for planar magnetics with natural convection
- Inductance: the air-gap is given by (38b) or (34b) depending if it is an inductance or a transformer respectively

the parameters left are controlled defining the design space below, and represented in Fig. 18:

- Air-gap l_g: discretized to the gap spacer thickness
- PCB track width p (window width): depending on the winding strategy, a minimum width in the window is required to fit the conductors
- Air-gap proximity to the windings s (window height): shorter windows tend to have higher winding losses due to the proximity of the gap (fringing) but making it higher will be translated into a deeper core (longer windings scaling winding losses proportionally)

B. Optimization

The optimization was performed via a smart algorithm capable of calculating the current excitations via a preliminary **Z** matrix obtained in ANSYS (refinement). This guarantees an accurate representation of the voltage between the winding terminals and thus, the core losses.

The design space was restricted according to the maximum dimensions of the machinery used in the manufacturing of the custom cores (less than 30 mm) as well as the height-constrained design (less than 12.9 mm) to achieve a half-brick form factor.

Fig. 19 shows the power losses as well as the winding strategy. Being the PSPSPSPSP better as the fringing effect gets more noticeable in the window (air-gap). At lower fringing fields, an additional parallel in the secondary reduces the R_{DC} enough to compensate for these effects.

The same core geometries were simulated for both the transformer and the inductor, for the final design of the three-phase inductor and transformer, the same custom core was chosen which dimensioning can be found in table IV and assembled by stacking cores (2 in the case of the transformer and 3 in the case of the inductor with 5 turns).

V. Implementation

A. Prototype

The final prototype is presented in Fig. 20 with its most important parts: complete power stage, three-phase transformer, three-phase inductor, the auxiliar supplies for the drivers and the signal isolators as well as their individual isolated DC/DC converters self-contained into the power stage.

The transistor selection for the first generation of the prototype is, for the high-voltage side inverter, the GS66508T from

TABLE IV: Optimized three-column EI-core dimensions

Parameter	Value	Description
w_w	7.1 mm	Window width
w_h	3.8 mm	Window height
A_f/d	4.5 mm	Junction column width
A_c/d	4.5 mm	Central column width
A_l/d	5.3 mm	Lateral column width
l_g	150 µm	Designed air-gap
d	8 mm	Depth of the core

GaN Systems (650 V, 30 A, 50 mΩ GaN E-HEMT) and for the rectifier, the BSZ018N04LS6 from Infineon (40 V, 158 A, 1.8 mΩ Si MOSFET).

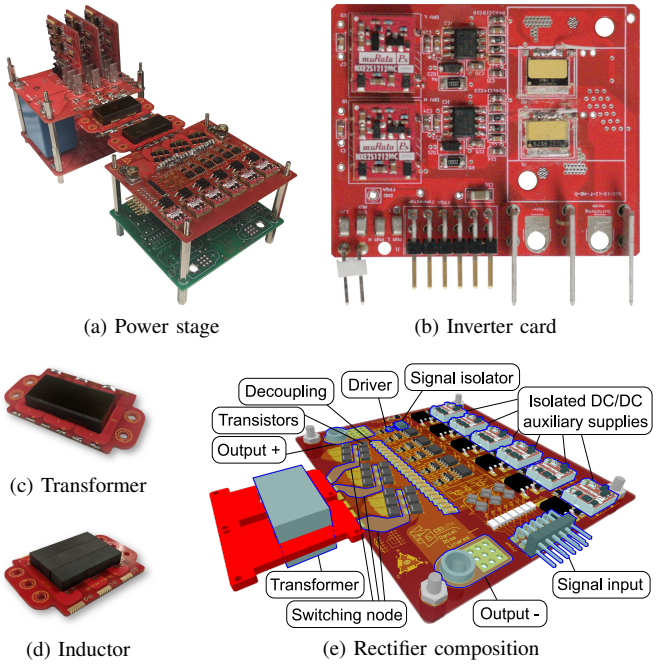

(a) Power stage (b) Inverter card

(c) Transformer

(d) Inductor

(e) Rectifier composition

Fig. 20: Prototype key parts

B. Transformer

The connection of the primary is trivial as there is no track entanglement in the PCB. Fig. 21 represents two possible solutions when creating the delta connection in the secondary of the transformer. Depending on the connection, the rectifier will lag the inverter by 30° or lead it by 30° (Yd11).

Both solutions are correct implementations of the topology. They deffer in the PCB layout execution (Fig. 21a is the most symmetric) and the modulation in the form of a delay.

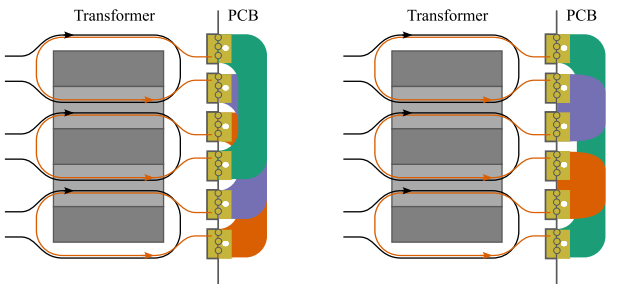

(a) Proposed connection (Yd1) (b) Alternative connection (Yd11)

Fig. 21: Delta connection on the secondary (Yd1/Yd11)

VI. Experimental Results

A. Operation of the converter

For aircraft applications, the heat is extracted via an isothermal baseplate at constant temperature (90 °C) integrated in a metal housing. As these conditions were not possible to replicate in the laboratory, it was tested with forced air convection at ambient temperature instead.

Fig. 22 shows the experimental waveforms of the converter for $f_S = 900\,\text{kHz}$, including the drain-source voltage of the low side transistors for each phase of the inverter (Fig. 22a) and rectifier (Fig. 22c), as well as the current waveforms through each resonant tank (Fig. 22b).

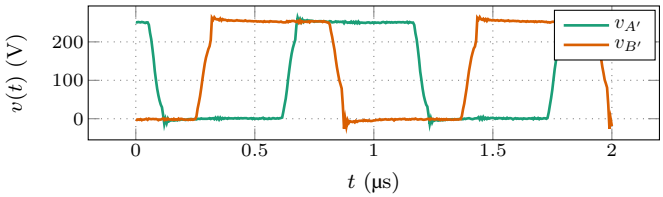

(a) Voltage at the switching nodes (resonant tank terminals)

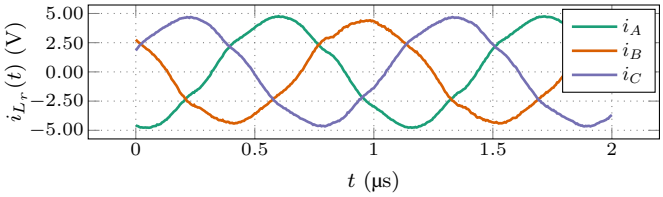

(b) Currents through the resonant tanks

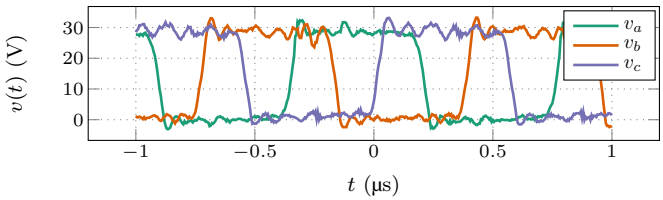

(c) Voltage at the switching nodes (delta terminals)

Fig. 22: Experimental waveforms for 250-28 V at 1 kW

Fig. 23 illustrates the dynamic ZVS (Zero Voltage Switching) transition characteristics experimentally, presenting the drain-source voltage and switching current for the full output power range (100 W and 1000 W).

The tests were not performed acting on the switching current, but by keeping the output voltage constant in an open-loop manner. The observed difference in switching currents between the two cases is attributed to the converter operating above resonance. While a higher switching frequency is necessary for lower power levels (Fig. 8) and hence increasing the inductive energy, higher load currents require the converter to adapt by adjusting the timing of the switching events (inverter-rectifier delay), resulting in proportionally higher currents

during the switching as the output power increases.

The effect of this off-current level is very subtle in the switching losses as demonstrated in [32].

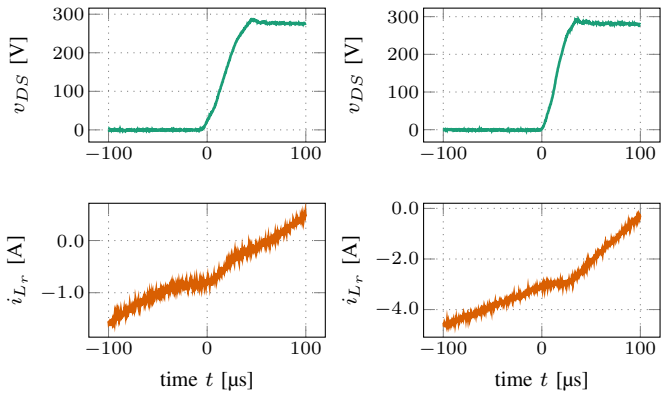

(a) $P_O = 100\,\mathrm{W}$ (b) $P_O = 1000\,\mathrm{W}$

Fig. 23: Inverter voltage ZVS transition at $V_I = 270\,\mathrm{V}$

B. Efficiency of the converter

The efficiency reached by this converter is over 95 % in the 333-1000 W output power range for the entire input voltage range with a maximum of 96 % at 580 W as shown in Fig. 24.

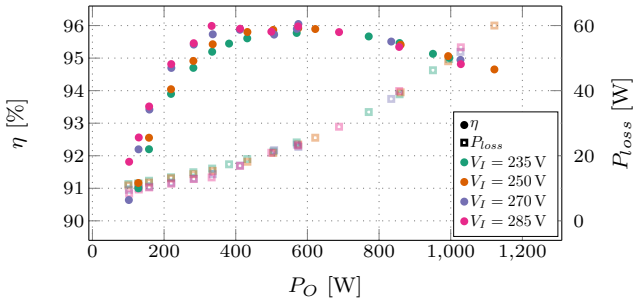

Fig. 24: Measured efficiency for 235-285 V of input voltage and the 100-1000 W output power range

All the experiments were made in an open-loop manner and tuning the frequency manually to obtain 28 V at the output (±1 %) with the input voltage constant within a 2 % of absolute maximum deviation.

The tests revealed a ±11 % of frequency variation for the ±15 % target, operating in the range 0.93-1.17 MHz. Fig. 25 shows a theoretical breakdown of the power losses at full load across the full range of input voltage levels (235-285 V) compared with experimental measurements. The conduction losses were calculated with the data provided by the manufacturer (on-resistance at the junction temperature), while the switching losses were obtained with the model and data in [32] for the inverter transistor Q_1-Q_6. As Q_7-Q_{12} are operated in Zero-Current Switching (ZCS), no voltage and current overlap losses are added due to the switching.

The most significant source of power losses is the inverter transistors, even though ZVS is present in the entire load range ($E_{on} = 0\,\mu\mathrm{J}$) as shown in Fig. 24, switching energy loss cannot be completely eliminated (E_{off}). This is because the transistor channel needs to be shut down as there will be simultaneous current and voltage across it during the transient.

The power losses for the magnetic components have been obtained from electromagnetic simulations and core loss measurements for trapezoidal B-field waveforms as explained in section IV.

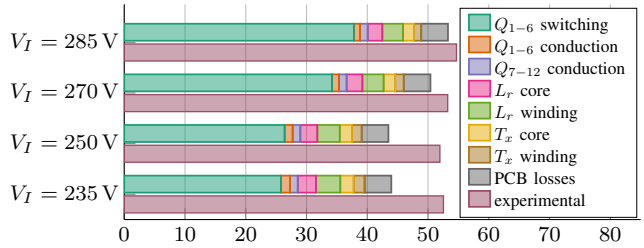

Fig. 25: Theoretical power losses breakdown comparison with experimental at $P_O = 1\,\mathrm{kW}$

C. Effect of the uncompensated magnetic core

With the help of an impedance analyzer and for the ML91S material from Proterial, the **Z** matrix was measured for both the transformer and the inductor obtaining an error not greater than a 5 % being the sensitivity of the μ_c of the material and the tolerance of the air-gap the sources subject to the most uncertainty.

The experimental inductance matrices according to (29a) for the transformer and (36) for the inductor are shown in (42) and (43) respectively.

$$\mathbf{L}_{T_x} = \begin{bmatrix} 12.90 & 2.56 & 7.00 & -1.44 & 5.16 & -1.07 \\ 2.55 & 0.52 & -1.43 & 0.29 & -1.06 & 0.22 \\ 7.00 & -1.43 & 14.56 & 2.88 & 6.80 & -1.40 \\ -1.44 & 0.29 & 2.88 & 0.59 & -1.40 & 0.29 \\ 5.15 & -1.06 & 6.80 & -1.40 & 12.68 & 2.50 \\ -1.07 & 0.22 & -1.40 & 0.28 & 2.50 & 0.51 \end{bmatrix} \mu\mathrm{H} \tag{42}$$

$$\mathbf{L}_{L_r} = \begin{bmatrix} 5.85 & 2.50 & 2.31 \\ 2.49 & 5.81 & 2.53 \\ 2.31 & 2.53 & 5.93 \end{bmatrix} \mu\mathrm{H} \tag{43}$$

In the analysis conducted in section III-A, a coupling factor of $k = 1$ was initially assumed. Based on the data in (42) and the single-phase equivalent described in (28), the coupling factor measured exceeds $k = 0.98$, thus validating the correctness of the initial assumption.

The most undesirable effect being given by the inductor L_r due to the series coupling when unbalanced. For this purpose, its error is calculated as the relative error of the main diagonal and the mutuals separately from (43):

$$\text{error} = \begin{bmatrix} -0.23\,\% & 2.20\,\% & -5.84\,\% \\ 1.81\,\% & -0.92\,\% & 3.36\,\% \\ -5.84\,\% & 3.36\,\% & 1.12\,\% \end{bmatrix} \tag{44}$$

The overall magnitude error when comparing it with the simulated and calculated is a 12 % lower, increasing the resonant frequency in a 6 %. The reason is given by numerous effects such as the unavoidable air-gap, the air-gap resolution, manufacturing tolerances in the manufacturing and the uncertainty in the permeability of the material.

Fig. 26 represents the effect of the compensation of the geometry to obtain a three-phase balanced system, showing

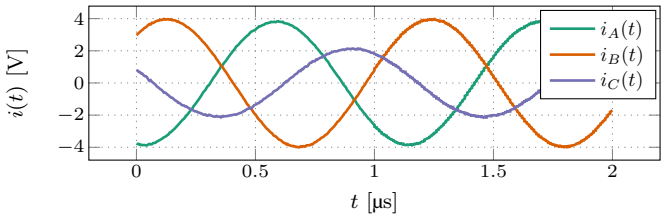

(a) Uncompensated inductor and transformer with the three legs equal ($|\Delta M/M| < 17\,\%$)

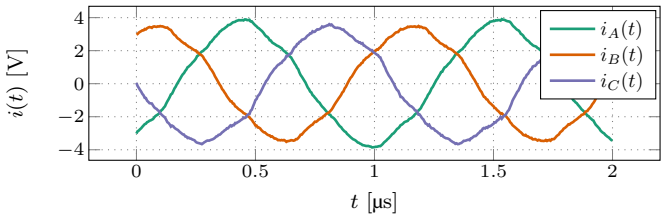

(b) Compensated inductor and transformer manufactured according to table IV ($|\Delta M/M| < 5\,\%$)

Fig. 26: Experimental waveforms for the inductor currents for different inductors (compensated and uncompensated)

once again that in the case of the three-phase magnetics the central leg must be tuned according to (23), and finally evaluating (38b) and (34b) to obtain the desired equivalent inductances (resonant and magnetizing respectively).

VII. Conclusions

In this paper, a DC/DC converter was designed, validated and built to fulfil the strict demands of aircraft applications. A wide input voltage (235 to 285 V), high-frequency (1 MHz) with a narrow operating frequency span (0.93 MHz to 1.17 MHz) achieving a $\pm 11\,\%$ in normal operation and with an output power of 1 kW.

Given that the nominal output voltage is 28 V, a high voltage step-down was required for which a three-phase LLC was proposed to lessen the RMS current per device and open up the design to three-phase transformers. In particular, the wye-delta configuration is the one that minimizes the number of turns of the primary leading to a smaller window and enabling the use of PCB windings.

The technique of placing as resonant inductors a three-phase inductor (and a single three-phase transformer) using 65 % of the copper (less number of turns required) and 60 % of the ferrite (single magnetic core) for the same specifications.

The main non-idealities of the magnetic components were address including the equivalent path length, the fringing effect as well as its effect on the different winding strategies in terms of losses. The reluctance model of EE and EI cores were derived, quantified via Finite Element simulation and experimentally demonstrated with a 5 % error allowing ZVS in the entire load range.

The system was tested for the entire input voltage range (235-285 V) and the output voltage range (100-1000 W) obtaining a 96 % maximum efficiency (power losses under 50 W).

With all the critical design features identified, a validated concept, accurate models and a working prototype, a smart

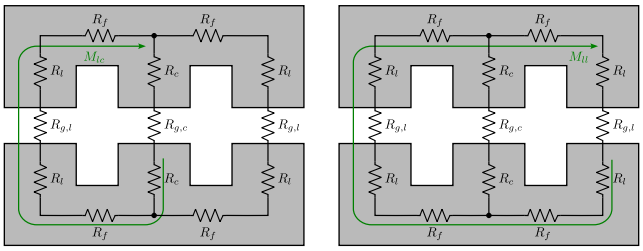

(a) M_{lc} calculation (b) M_{ll} calculation

Fig. 27: Reluctance model

optimization at system-level and component-level can be performed. Guidelines to model and design the system are yet to be listed and analyzed in depth in future research work.

Acknowledgements

We gratefully acknowledge Hitachi Metals for their invaluable contribution to this research, providing high-quality ferrite cores that played a crucial role in the experimental work presented in this paper. We extend our appreciation for their commitment to scientific progress and technological innovation.

Special thanks to the Princeton University Team that allowed us to test our magnetic components particularly to Diego Serrano López who made the measurements.

Appendix A
Reluctance Model of an EE Core

A significant aspect that requires careful consideration is the design of the magnetic core structure. In particular, the transformer employs a non-symmetrical configuration with three independent magnetic paths corresponding to the three columns.

To this end, and to complement the magnetostatic model detailed in section III-A, a reluctance model is employed to equalize the mutual inductances between columns. By analyzing the magnetic flux distribution, a compensation technique is introduced. This compensation involves narrowing the central column while having two identical lateral columns, effectively altering the magnetic paths to achieve balanced coupling.

As a result, the equivalent reluctance model ensures that the mutual inductances become equivalent in the lateral-to-central and lateral-to-lateral loops, obtaining a balanced interaction between the phases. This optimized configuration leads to reduced power losses, improved thermal stability, and enhanced overall efficiency of the Three-Phase LLC resonant converter.

For this regard, Hopkinson's Law is applied for every section of the magnetic core,

$$R_f = \frac{l_a}{\mu_0 \mu_r A_f} \tag{45a}$$

$$R_l = \frac{l_b}{\mu_0 \mu_r A_l}, \; R_c = \frac{l_b}{\mu_0 \mu_r A_c} \tag{45b}$$

$$R_{g,l} = \frac{l_g}{\mu_0 \sigma_l A_l}, \; R_{g,c} = \frac{l_g}{\mu_0 \sigma_c A_c} \tag{45c}$$

and to have $M_{lc} \equiv M_{ll}$, the sum of the reluctances along the magnetic paths drawn in green for Fig. 27 must be equal:

$$2R_c + R_{g,c} = 2R_f + 2R_l + R_{g,l} \tag{46}$$

resulting in the same expression as in (23):

$$A_l^* = A_c \cdot \frac{A_f \left(2\frac{l_b}{\mu_c} + \frac{l_g}{\sigma_l} \right)}{A_f \left(2\frac{l_b}{\mu_c} + \frac{l_g}{\sigma_c} \right) - 2A_c \frac{l_a}{\mu_c}} \tag{47}$$

REFERENCES

[1] Mohd Tariq, Ali I. Maswood, Chandana Jayampathi Gajanayake, et al. "Modeling and Integration of a Lithium-Ion Battery Energy Storage System With the More Electric Aircraft 270 V DC Power Distribution Architecture". In: *IEEE Access* 6 (2018), pp. 41785–41802. ISSN: 2169-3536. DOI: 10.1109/ACCESS.2018.2860679.

[2] Bor-Ren Lin and Huei-Yuan Shih. "ZVS Converter With Parallel Connection in Primary Side and Series Connection in Secondary Side". In: *IEEE Transactions on Industrial Electronics* 58.4 (2011), pp. 1251–1258. DOI: 10.1109/TIE.2010.2042422.

[3] Bor-Ren Lin and Jia-Yu Dong. "ZVS Resonant Converter With Parallel–Series Transformer Connection". In: *IEEE Transactions on Industrial Electronics* 58.7 (2011), pp. 2972–2979. DOI: 10.1109/TIE.2010.2077612.

[4] Bor-Ren Lin and Shin-Feng Wu. "ZVS Resonant Converter With Series-Connected Transformers". In: *IEEE Transactions on Industrial Electronics* 58.8 (2011), pp. 3547–3554. DOI: 10.1109/TIE.2010.2089946.

[5] Aurora de Juan, Diego Serrano, Pedro Alou, et al. "High-Frequency LLC Converter with Narrow Frequency Variations for Aircraft Applications". In: *2022 IEEE Applied Power Electronics Conference and Exposition (APEC)*. 2022, pp. 2098–2105. DOI: 10.1109/APEC43599.2022.9773409.

[6] Shahid Iqbal. "Interleaved LLC resonant converter with integrated dual transformer for PV power systems". In: *8th IET International Conference on Power Electronics, Machines and Drives (PEMD 2016)*. 2016, pp. 1–6. DOI: 10.1049/cp.2016.0209.

[7] Guangcan Li and Xinke Wu. "A 98.4% 380V-12V DCX With 1.3kW/in3 Power Density Using Low NFoM Devices and Resonant Drive Transformer". In: *IEEE Transactions on Power Electronics* 37.10 (2022), pp. 12346–12356. DOI: 10.1109/TPEL.2022.3178162.

[8] Gustavo C. Knabben, Grayson Zulauf, Jannik Schäfer, et al. "Conceptualization and Analysis of a Next-Generation Ultra-Compact 1.5-kW PCB-Integrated Wide-Input-Voltage-Range 12V-Output Industrial DC/DC Converter Module". In: *Electronics* 10.17 (2021). ISSN: 2079-9292. DOI: 10.3390/electronics10172158. URL: https://www.mdpi.com/2079-9292/10/17/2158.

[9] Ren Ren, Bo Liu, Edward A. Jones, et al. "Capacitor-Clamped, Three-level GaN-Based DC–DC Converter With Dual Voltage Outputs for Battery Charger Applications". In: *IEEE Journal of Emerging and Selected Topics in Power Electronics* 4.3 (2016), pp. 841–853. DOI: 10.1109/JESTPE.2016.2586890.

[10] Tianyang Jiang, Junming Zhang, Xinke Wu, et al. "A Bidirectional Three-Level LLC Resonant Converter With PWAM Control". In: *IEEE Transactions on Power Electronics* 31.3 (2016), pp. 2213–2225. DOI: 10.1109/TPEL.2015.2438072.

[11] Jing-Yuan Lin, Hsuan-Yu Yueh, Yi-Feng Lin, et al. "Analysis and Design of Three-Phase LLC Resonant Converter with Matrix Transformers". In: *Energies* 15 (Feb. 2022), p. 1315. DOI: 10.3390/en15041315.

[12] Enrico Orietti, Paolo Mattavelli, Giorgio Spiazzi, et al. "Current sharing in three-phase LLC interleaved resonant converter". In: *2009 IEEE Energy Conversion Congress and Exposition*. 2009, pp. 1145–1152. DOI: 10.1109/ECCE.2009.5316510.

[13] Yucen Li, Shuai Shao, Hui Chen, et al. "High-gain high-efficiency IPOS LLC converter with coupled transformer and current sharing capability". In: *CPSS Transactions on Power Electronics and Applications* 5.1 (2020), pp. 63–73. DOI: 10.24295/CPSSTPEA.2020.00006.

[14] Rimon Gadelrab, Ahmed Nabih, Fred C. Lee, et al. "LLC Resonant Converter with 99 Efficiency for Data Center Server". In: *2021 IEEE Applied Power Electronics Conference and Exposition (APEC)*. 2021, pp. 310–319. DOI: 10.1109/APEC42165.2021.9487423.

[15] Chao Fei, Rimon Gadelrab, Qiang Li, et al. "High-Frequency Three-Phase Interleaved LLC Resonant Converter With GaN Devices and Integrated Planar Magnetics". In: *IEEE Journal of Emerging and Selected Topics in Power Electronics* 7.2 (2019), pp. 653–663. DOI: 10.1109/JESTPE.2019.2891317.

[16] R. Mirzahosseini and F. Tahami. "A phase-shift three-phase bidirectional series resonant DC/DC converter". In: *IECON 2011 - 37th Annual Conference of the IEEE Industrial Electronics Society*. 2011, pp. 1137–1143. DOI: 10.1109/IECON.2011.6119468.

[17] Rimon Gadelrab and Fred C. Lee. "PCB-Based Magnetic Integration and Design Optimization for Three-Phase LLC". In: *IEEE Transactions on Power Electronics* 38.11 (2023), pp. 14037–14049. DOI: 10.1109/TPEL.2023.3285652.

[18] Hiroaki Matsumori, Toshihisa Shimizy, Koushi Takano, et al. "Three-Phase AC Filter Inductor Design for Three-Phase PWM Inverter for Conversion Efficiency Improvement at Low Load". In: *Electrical Engineering in Japan* 203.1 (2018), pp. 37–49. DOI: https://doi.org/10.1002/eej.23053.

[19] Mostafa Noah, Shota Kimura, Jun Imaoka, et al. "Magnetic Design and Experimental Evaluation of a Commercially Available Single Integrated Transformer in Three-Phase LLC Resonant Converter". In: *IEEE Transactions on Industry Applications* 54.6 (2018), pp. 6190–6204. DOI: 10.1109/TIA.2018.2856631.

[20] Anup Anurag, Sayan Acharya, Subhashish Bhattacharya, et al. "A Gen-3 10-kV SiC MOSFET-Based Medium-Voltage Three-Phase Dual Active Bridge Converter Enabling a Mobile Utility Support Equipment Solid State Transformer". In: *IEEE Journal of Emerging and Selected Topics in Power Electronics* 10.2 (2022), pp. 1519–1536. DOI: 10.1109/JESTPE.2021.3069810.

[21] Aurora de Juan, Diego Serrano, Pedro Alou, et al. "Analytical Modelling of Single-Phase and Three-Phase DC/DC LLC Converters". In: *2022 IEEE Applied Power Electronics Conference and Exposition (APEC)*. 2022, pp. 2106–2113. DOI: 10.1109/APEC43599.2022.9773467.

[22] Xiang Fang, Haibing Hu, Z. John Shen, et al. "Operation Mode Analysis and Peak Gain Approximation of the LLC Resonant Converter". In: *IEEE Transactions on Power Electronics* 27.4 (2012), pp. 1985–1995. DOI: 10.1109/TPEL.2011.2168545.

[23] Veda Samhitha Duppalli and Scott Sudhoff. "Power density comparison of three-phase AC inductor architectures". In: *2017 IEEE Electric Ship Technologies Symposium (ESTS)*. 2017, pp. 217–224. DOI: 10.1109/ESTS.2017.8069284.

[24] A. Balakrishnan, W.T. Joines, and T.G. Wilson. "Air-gap reluctance and inductance calculations for magnetic circuits using a Schwarz-Christoffel transformation". In: *IEEE Transactions on Power Electronics* 12.4 (1997), pp. 654–663. DOI: 10.1109/63.602560.

[25] J. Muhlethaler, J. W. Kolar, and A. Ecklebe. "A novel approach for 3d air gap reluctance calculations". In: *8th International Conference on Power Electronics - ECCE Asia*. 2011, pp. 446–452. DOI: 10.1109/ICPE.2011.5944575.

[26] Haoran Li, Seungjae Ryan Lee, Min Luo, et al. "MagNet: A Machine Learning Framework for Magnetic Core Loss Modeling". In: *2020 IEEE 21st Workshop on Control and Modeling for Power Electronics (COMPEL)*. 2020, pp. 1–8. DOI: 10.1109/COMPEL49091.2020.9265869.

[27] Jannik Schäfer, Dominik Bortis, and Johann W. Kolar. "Novel Highly Efficient/Compact Automotive PCB Winding Inductors Based on the Compensating Air-Gap Fringing Field Concept". In: *IEEE Transactions on Power Electronics* 35.9 (2020), pp. 9617–9631. DOI: 10.1109/TPEL.2020.2969295.

[28] Mike K. Ranjram, Pedro Acosta, and David J. Perreault. "Design Considerations for Planar Magnetic Terminations". In: *2019 20th Workshop on Control and Modeling for Power Electronics (COMPEL)*. 2019, pp. 1–8. DOI: 10.1109/COMPEL.2019.8769642.

[29] Marian Kazimierczuk. *High-Frequency Magnetic Components: Second Edition*. Nov. 2013, pp. 1–729. ISBN: 9781118717790. DOI: 10.1002/9781118717806.

[30] Rouhollah Shafaei, Maria Celeste Garcia Perez, and Martin Ordonez. "Planar Transformers in LLC Resonant Converters: High-Frequency Fringing Losses Modeling". In: *IEEE Transactions on Power Electronics* 35.9 (2020), pp. 9632–9649. DOI: 10.1109/TPEL.2020.2971424.

[31] Yuliang Cao, Minh Ngo, Ning Yan, et al. "Design and Implementation of an 18-kW 500-kHz 98.8 Efficiency High-Density Battery Charger With Partial Power Processing". In: *IEEE Journal of Emerging and Selected Topics in Power Electronics* 10.6 (2022), pp. 7963–7975. DOI: 10.1109/JESTPE.2021.3108717.

[32] Edward A. Jones, Fred Wang, Daniel Costinett, et al. "Characterization of an enhancement-mode 650-V GaN HFET". In: *2015 IEEE Energy Conversion Congress and Exposition (ECCE)*. 2015, pp. 400–407. DOI: 10.1109/ECCE.2015.7309716.

Daniel Ríos Linares (Student Member, IEEE) received the B.Ss. degree in industrial electronics engineering, University of Granada, Spain in 2019, and his M.Sc. from Universidad Politécnica de Madrid (UPM), Madrid, Spain, in 2021. He is currently pursuing his Ph.D. degree at Centro de Electrónica Industrial (CEI) at UPM. His areas of interests are the design of DC/DC power converters, topologies and optimization of high-frequency applications.

Alberto Delgado Expósito (Member, IEEE) received the B.Sc. degree in electrical engineering from the University of Malaga, Malaga, Spain, in 2016, and the M.Sc. and Ph.D. degrees in industrial electronics from the Polytechnic University of Madrid (UPM), Madrid, Spain, in 2017 and 2021, respectively. He became a Teaching Assistant with UPM in 2019. His research interests include modeling of dc– dc converters for inductive power transfer systems and magnetic components for different applications, such as RFID communications and wireless charging and magnetic nanomaterials and micromaterials. Dr. Delgado was a recipient of the Best Student of the Year Award and honors on several occasions, during his undergraduate studies

Miroslav Vasić (Senior Member, IEEE) was born in Serbia in 1981. He received the B.S. degree in electrical engineering from the School of Electrical Engineering, University of Belgrade, Belgrade, Serbia, and the M.S. and Ph.D. degrees in industrial electronics from Centro de Electronica Industrial, Escuela Tecnica Superior de Ingenieros Industriales (ETSII), Universidad Politécnica de Madrid (UPM), Madrid, Spain, in 2005, 2007, and 2010, respectively. Since then, he has been with Centro de Electronica Industrial, ETSII, UPM. He has been working as an Associate Professor with UPM since 2019. His research interests include the application of power converters and their optimization. In recent years, a great part of his research activities has been related to the research of new semiconductor devices based on GaN and their impact on power electronics. He has authored or coauthored more than 70 peer-reviewed technical papers at conferences and in IEEE journals and he advised five Ph.D. thesis and holds six patents. Dr. Vasić was a recipient of the Semikron Innovation Award for the teamwork on "RF Power Amplifier With Increased Efficiency and Bandwidth" in 2012, a medal from the Spanish Royal Academy of Engineering as a recognition of his research trajectory in 2015, and UPM Research Projection Award for the best young Researcher at Universidad Politecnica de Madrid, in 2016. He actively serves as an Associate Editor for the *IEEE Journal of Emerging and Selected Topics in Power Electronics* and *IEEE transactions on vehicular technology*. He was one of the cofounders of the IEEE PELS TC 10-Design Methodologies and acted as the Vice-Chair from 2021 until 2023.